

Self-similarity among energy eigenstates

Zhelun Zhang (张哲伦)^{1,*}, Zhenduo Wang (王朕铎)^{1,*} and Biao Wu (吴飙)^{1,2,3}

¹International Center for Quantum Materials, School of Physics, Peking University, Beijing 100871, China

²Wilczek Quantum Center, School of Physics and Astronomy, Shanghai Jiao Tong University, Shanghai 200240, China

³Collaborative Innovation Center of Quantum Matter, Beijing 100871, China



(Received 23 October 2022; accepted 21 February 2023; published 15 March 2023)

In a quantum system, different energy eigenstates have different properties or features, allowing us to define a classifier to divide them into different groups. We find that the ratio of each type of energy eigenstate in an energy shell $[E_c - \Delta E/2, E_c + \Delta E/2]$ is invariant with changing width ΔE or Planck constant \hbar as long as the number of eigenstates in the shell is statistically large enough. We give an argument that such self-similarity in energy eigenstates is a general feature for all quantum systems, which is further illustrated numerically with various quantum systems, including circular billiard, double top model, kicked rotor, and Heisenberg XXZ model.

DOI: [10.1103/PhysRevE.107.034123](https://doi.org/10.1103/PhysRevE.107.034123)

I. INTRODUCTION

Energy eigenvalues and eigenstates are constitutive to the properties of quantum systems. They have already been thoroughly studied in various aspects. For eigenvalues, the well-known results include the Weyl law [1] and its generalization [2–10], which describes the asymptotic behavior of the number of energy eigenvalues below an increasing energy. The distribution of nearest energy level spacings [11–17] is now widely used to characterize quantum systems: Wigner-Dyson distribution for chaotic systems and Poisson distribution for integrable systems. The degeneracy in eigenenergies and their differences has been shown to be related to ergodicity and mixing in quantum systems [18–20].

For energy eigenstates, there are also many interesting results. These earliest studies have focused on the correlation and amplitude distribution of a single energy eigenstate [11,21–27]. This line of studies ultimately leads to a well-known hypothesis by Berry: Each energy eigenstate has a Wigner function concentrated on the region explored by a typical orbit over infinite times in the semiclassical limit, or, equivalently, each energy eigenstate becomes a minimal invariant ensemble distribution in classical phase space in the semiclassical limit [28]. Recently, there have been studies on the single energy eigenstate in spin systems, which have no well-defined semiclassical limit [29–35].

In this work we focus on a sequence of energy eigenstates in an energy shell $\mathcal{S}(E_c, \Delta E) = [E_c - \Delta E/2, E_c + \Delta E/2]$. As these eigenstates have different physical properties or features, we define a classifier for a given physical property or feature and divide these eigenstates into different groups. We find self-similarity among energy eigenstates for all quantum systems in the following sense: If the ratio of the energy eigenstates having property A is f in the energy shell $\mathcal{S}(E_c, \Delta E)$, then the ratio is still f in the

subshell $\mathcal{S}(E'_c, \Delta E') \subset \mathcal{S}(E_c, \Delta E)$ as long as the number of eigenstates in the subshell is statistically large enough. The self-similarity is particularly pronounced in the semiclassical limit $\hbar \rightarrow 0$, where the number of eigenstates in a very narrow energy shell is very large.

We first illustrate such self-similarity with a simple model, circular billiard with analytical results, and extensive numerical computation. We then give an analysis, arguing that such self-similarity is a generic feature for any quantum system that has a well-defined semiclassical limit. We finally illustrate the self-similarity with more examples, which include coupled tops, kicked rotor, and the Heisenberg XXZ model. The result for the XXZ model is of particular interest as it shows that the self-similarity exists even in quantum systems that have no well-defined semiclassical limits. In the end, we argue that such a self-similarity offers a good explanation why the microcanonical ensemble in quantum statistical mechanics, which is established on the equal probability hypothesis, works for all quantum systems regardless of their integrability.

II. SELF-SIMILARITY IN ENERGY EIGENSTATES

Before general discussion, we study a simple but illustrative example, a quantum circular billiard [36], where the self-similarity in its energy eigenstates can be demonstrated convincingly through analysis and extensive numerical calculation.

A. Circular billiard

For a quantum particle of mass M moving in a circular billiard of radius R_0 , its energy eigenstates can be expressed analytically in terms of the Bessel function J_m ,

$$\psi_{nm}(r, \theta) = \frac{1}{\sqrt{\pi R_0 |J'_m(k_{nm} R_0)|}} J_m(k_{nm} r) e^{im\theta}, \quad (1)$$

where n is the radial quantum number and m is the angular quantum number with k_{nm} being determined by the boundary

*These two authors contributed equally to this work.

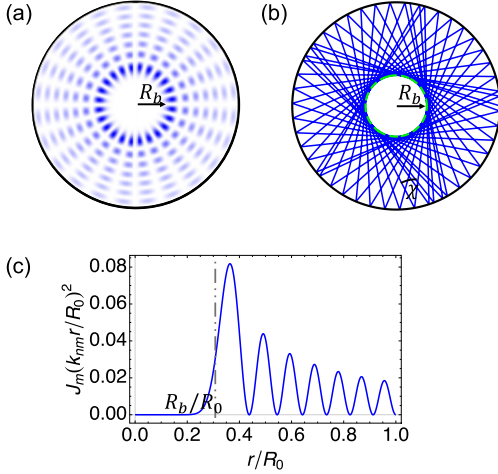


FIG. 1. Circular billiard. (a) A typical quantum energy eigenfunction $|\psi_{nm} + \psi_{n,-m}|^2/2$, (b) a typical classical trajectory, and (c) the square of a Bessel function $J_m(k_{nm}r)$ with R_b indicated. In this figure, $n = 7$ and $m = 12$.

condition

$$J_m(k_{nm}R_0) = 0. \quad (2)$$

It is clear that $|\psi_{nm})$ and $|\psi_{n,-m})$ are degenerate with the same eigenenergy of $E_{nm} = \hbar^2 k_{nm}^2 / (2M)$. For simplicity, we choose the units in which $\hbar = M = 1$ in the following discussion.

A typical energy eigenfunction is plotted in Fig. 1(a). An obvious feature is that the eigenfunction $|\psi_{nm})$ (or any linear superposition of $|\psi_{nm})$ and $|\psi_{n,-m})$) is almost zero inside a circle of a certain radius R_b . The corresponding classical motion has a similar “blank region.” As one can see clearly from Fig. 1(b), for a classical particle bouncing elastically inside the circular billiard, if its initial angular momentum is MvR_b , then it never moves inside the circle of radius R_b . Since the motion of a classical particle in a billiard is independent of the size of its momentum Mv , the radius R_b of such a blank region can be regarded as a kind of normalized angular momentum. With this understanding in mind, for an energy eigenstate $|\psi_{nm})$, we define a normalized angular momentum \mathfrak{R}_{nm} as

$$\mathfrak{R}_{nm} = \frac{\langle \psi_{nm} | L_z | \psi_{nm} \rangle}{\sqrt{2E_{nm}}} = \frac{m}{k_{nm}}. \quad (3)$$

As indicated in Fig. 1(c), \mathfrak{R}_{nm} defined in such a way can be regarded as the radius of the “blank region” of $|\psi_{nm})$.

Our discussion above shows that the radius \mathfrak{R}_{nm} can be used to characterize the eigenstate $|\psi_{nm})$. To be precise, we introduce a classifier,

$$C(R_b; |\psi_{nm})) = \begin{cases} 1 & \text{if } 0 < \mathfrak{R}_{nm} < R_b, \\ 0 & \text{if } R_b \leq \mathfrak{R}_{nm} < R_0. \end{cases} \quad (4)$$

It says that if the radius \mathfrak{R}_{nm} of an eigenstate $|\psi_{nm})$ is smaller than R_b , then $C(R_b; |\psi_{nm})) = 1$; otherwise, it is zero. We consider an energy shell $\mathcal{S}(E_c, \Delta E) = [E_c - \Delta E/2, E_c + \Delta E/2]$, which is centered at E_c and with a width of ΔE . We are interested in how many eigenstates in the shell $\mathcal{S}(E_c, \Delta E)$ have their blank region radii $\mathfrak{R}_{nm} < R_b$. For this purpose, we

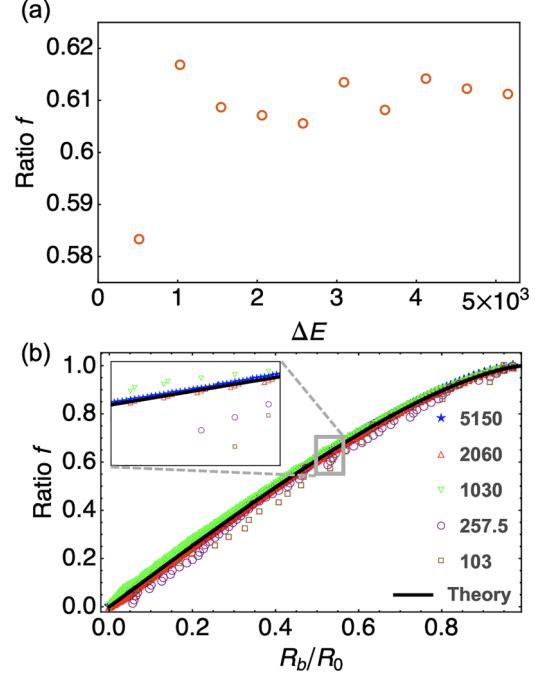


FIG. 2. (a) Ratio $f(R_0/2; E_c, \Delta E)$ as a function of ΔE . (b) Ratio $f(R_b/R_0; E_c, \Delta E)$ as a function of R_b/R_0 . In this numerical results, we take $\hbar = 1$ and fix $k_c = 515$ (corresponding $E_c = k_c^2/2$), while changing Δk from 0.1 to 5 (corresponding $\Delta E = 2k_c \Delta k$). The narrowest energy window (i.e., $\Delta k = 0.2$) has merely 28 energy eigenstates, and thus Δk cannot be further narrowed. Here we plot the ratio of energy eigenstates with “blank region radius” less than R_b vs. R_b . Except for $\Delta k = 0.1$ and 0.25 (i.e., energy window is too narrow), other curves (with moderate or large energy window) embody a perfect self-similarity. The black line represents the theoretical result Eq. (8).

define a ratio

$$f(R_b; E_c, \Delta E) = \frac{\sum_{E_{nm} \in \mathcal{S}} C(R_b; |\psi_{nm}))}{\text{number of eigenstates in } \mathcal{S}}. \quad (5)$$

We have numerically computed the ratio $f(R_b; E_c, \Delta E)$. One set of the results are plotted in Fig. 2(a), which shows how the ratio $f(R_b; E_c, \Delta E)$ changes with ΔE with R_b fixed at $R_0/2$. It is clear from this figure that the ratio f stays almost constant once the shell width ΔE is large enough. For this specific example, the figure shows that in a not-too-narrow energy shell, there are always about 61% of the eigenfunctions $|\psi_{nm})$ whose blank region radius R_b is smaller than $R_0/2$. This is self-similarity. Figure 2(b) shows that this kind of self-similarity exists for all values of R_b not just for $R_b = R_0/2$. In particular, as seen from this figure, the curves $f(R_b; E_c, \Delta E)$ for different widths ΔE approach a limiting curve when ΔE increases. Note that the above results are not sensitive to the center E_c of the energy shell as long as it is not too close to the ground state.

For any quantum system, when \hbar becomes smaller, more energy eigenstates enter an energy shell $\mathcal{S}(E_c, \Delta E)$ with fixed center E_c and width ΔE (see Fig. 3). For this billiard system, as its eigenenergy $E_{nm} = \hbar^2 k_{nm}^2 / (2M)$, decreasing \hbar reduces the gap between the nearest energy levels and is roughly equivalent to enlarge the width of energy shell. (See

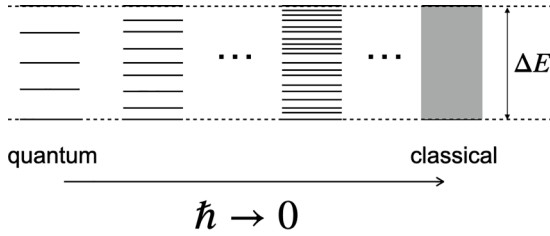


FIG. 3. As the Planck constant \hbar becomes smaller, more energy eigenstates enter a given energy shell. In the semiclassical limit $\hbar \rightarrow 0$, the energy spectrum becomes continuous.

Appendix A for a detail discussion of the relation between decreasing \hbar and increasing ΔE .) Therefore, the self-similarity demonstrated in Fig. 2 implies that at the smaller Planck constant, the fraction of $f(R_b; \Delta E)$ would get little changed. Since the system becomes classical in the limit of $\hbar \rightarrow 0$, the limit of the ratio $f(R_b; \Delta E)$ is likely to have a classical interpretation. This is indeed the case as we shall see.

Let us consider the classical circular billiard. For a classical system, the energy shell $S(E_c, \Delta E)$ specifies a volume in its phase space. For a billiard system, as its dynamics is the same for all different energies, we can focus on an isoenergetic surface in the volume. We define another ratio

$$g(R_b; E) = \frac{\int_{<R_b} dx dy dp_x dp_y}{\int_T dx dy dp_x dp_y}. \quad (6)$$

Here the nominator is the phase-space volume of a constant energy surface with energy $E = p^2/2$. For the trajectories in a classical billiard are the same for different momentum, we take $p = 1$ for simplicity. The denominator is the volume occupied by all the trajectories with blank region radius smaller than R_b . For a trajectory starting at point $\mathbf{r} = (x, y)$ in the circular billiard, it is completely determined by the direction of its momentum \mathbf{p} . For this trajectory to enter the circle of radius R_b , the direction of its motion must be limited in the angle $\alpha(x, y; R_b) = 2 \arcsin(R_b/r)$, where $r = \sqrt{x^2 + y^2}$, as

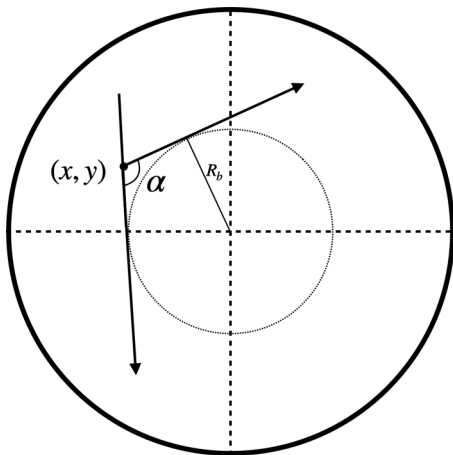


FIG. 4. In a classical circular billiard, for a particle starting at $\mathbf{r} = (x, y)$, only when its direction of motion is limited inside the angle of α can it enter a circle of radius of R_b . Otherwise, it always stays outside of the circle.

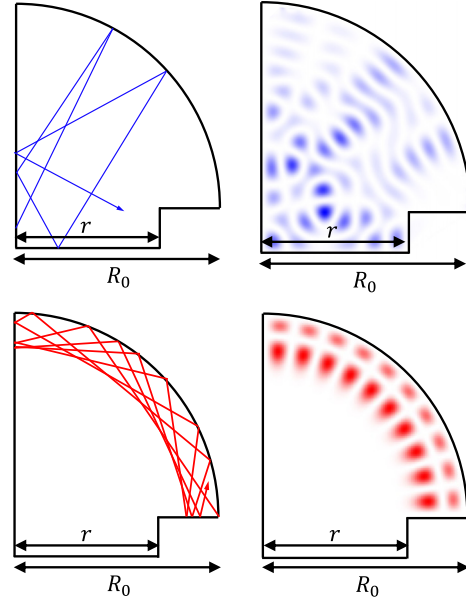


FIG. 5. Mushroom billiard which is made of a quarter of circle and a rectangle. For the motion with the blank region radius R_b smaller than r , the horizontal length of the rectangle, it is chaotic; otherwise, it is integrable.

shown in Fig. 4. As a result, we have

$$g(R_b) = \frac{\int_{r < R_b} \alpha(x, y; R_b) dx dy}{\pi \int_{0 < r < R_0} dx dy}. \quad (7)$$

Evaluating this integral in the polar coordinate, we obtain

$$g(R_b) = \frac{2}{\pi} (u \sqrt{1 - u^2} + \arcsin u), \quad (8)$$

where $u = R_b/R_0$. This theoretical result is plotted as a black line in Fig. 2(b), where we see that it agrees very well with our numerical results for $f(R_b; E_c, \Delta E)$.

The circular billiard is an integrable system, but our results can be safely generalized for nonintegrable or chaotic systems. The mushroom billiard in Fig. 5, which is obtained by adding a rectangular stalk to a quarter of circle, is a nonintegrable system, which has both integrable motions and chaotic motions [37]. When the blank region radius or normalized angular momentum R_b is bigger than r , the motion is integrable; otherwise, it is chaotic. We find that the number of chaotic energy eigenstates, e.g., the one in the upper-right corner of Fig. 5, in an energy shell is proportional to the volume of chaotic trajectories in the classical phase space. For this system, R_b is an indicator of chaotic motion.

B. General discussion

With the circular billiard, we have found a self-similarity in energy eigenstates that is intimately related to the classical dynamics. This is in fact a general feature that exists in all quantum systems as our analysis below shows.

We consider a general quantum system, which has a well-defined classical counterpart. Its quantum phase space can be obtained by dividing the classical phase space into Planck cells [38] as shown in Fig. 6. An energy shell $S(E_c, \Delta E)$

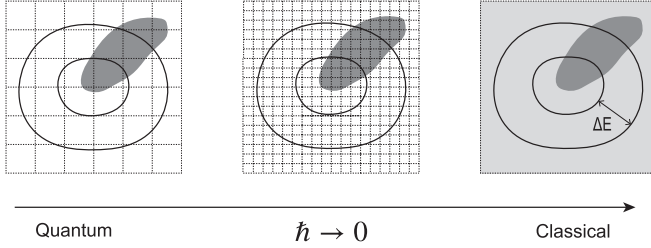


FIG. 6. The schematic of a quantum system approaching its semiclassical limit $\hbar \rightarrow 0$ in phase space. The two black curves represent two constant energy surfaces with difference ΔE ; the area enclosed by them are the volume of a given energy shell $\mathcal{S}(E_c, \Delta E)$. The dark shaded area is a region where the system has a certain physical property A . As \hbar decreases toward zero, the Planck cells (squares in the figure) become smaller. As a result, there are more energy eigenstates in the energy shell $\mathcal{S}(E_c, \Delta E)$ and more eigenstates have property A . However, the proportional of energy eigenstates having property A in the energy shell $\mathcal{S}(E_c, \Delta E)$ quickly approach a limit, which is the overlap of the energy shell and the dark area.

in phase space is a volume enclosed by two constant energy surfaces around E_c , which are plotted as two black curves in Fig. 6. The dark shaded area in the figure is a collection of all the states (quantum or classical) that have physical property A . For the above example of the circular billiard, the property A is the blank region radius smaller than R_b . According to quantum mechanics, the number of Planck cells in a phase-space volume is the same as the number of energy eigenstates [39]. As a result, the number of energy eigenstates with property A in the energy shell $\mathcal{S}(E_c, \Delta E)$ is equal to the number of Planck cells in the overlap region, the dark area between two black curves in Fig. 6. When \hbar decreases, the Planck cells become smaller so that the number of energy eigenstates in different categories, e.g., in an energy shell or having property A , increases. However, the ratio between numbers in these different categories will quickly saturate and reach a limit that is set by the ratio between volumes of corresponding categories in the classical phase space. For the circular billiard, the former is $f(R_b; E_c, \Delta E)$ and the latter is $g(R_b; E_c)$.

The above analysis motivates us to generalize the classifier C and related ratio f in Eqs. (4) and (5). For a given quantum system, a classifier C maps its energy eigenstates into binary value $C(|E\rangle) \in \{0, 1\}$, that is, divides the eigenstates into two groups. Formally, we can write

$$C(\xi; |E\rangle) = \begin{cases} 0 & \mathcal{A}(|E\rangle) < \xi \\ 1 & \mathcal{A}(|E\rangle) \geq \xi \end{cases}, \quad (9)$$

where \mathcal{A} is a function that characterizes physical property A of an eigenfunction $|E\rangle$ and ξ is a certain value. The choice of property A and related function \mathcal{A} depends on the quantum system that is being considered. For the circular billiard, we have chosen the blank region radius R_b and related function Re_{nm} . For a quantum chaotic system, one possible choice is the effective occupation $\mathcal{A}(|E\rangle) = (\sum_x |\langle x|E\rangle|^4)^{-1}$ [40], which characterizes how widely a wave function spreads in space. More examples will be given later. Note that one can certainly define a classifier that maps the energy eigenstates

into three or more groups. We for simplicity focus on the above definition.

For an energy shell $\mathcal{S}(E_c, \Delta E, \hbar) = \{|E\rangle : E \in [E_c - \Delta E/2, E_c + \Delta E/2]\}$, with the above classifier, we define the following ratio:

$$f(\wp, E_c, \Delta E) = \frac{\sum_{|E\rangle \in \mathcal{S}} C(|E\rangle)}{\text{number of eigenstates in } \mathcal{S}}. \quad (10)$$

Here \wp is a parameter that controls the number of energy eigenstates in the energy shell $\mathcal{S}(E_c, \Delta E)$. When the quantum system has a well-defined classical limit, \wp is just the Planck constant \hbar or the effective Planck constant. The self-similarity in energy eigenstates means that the ratio $f(\wp, E_c, \Delta E)$ is independent of the control parameter \wp and the width ΔE as long as the number of eigenstates in the shell \mathcal{S} is statistically large enough. In particular, one can divide the shell \mathcal{S} into many small subshells and tune the control parameter \wp so that each subshell contains enough energy eigenstates. In this case, within statistical fluctuations, the ratio f is the same for every subshell.

The ratio $f(\wp, E_c, \Delta E)$ has a weak dependence on E_c , the center of the energy shell. By weak dependence, we mean that $f(\wp, E_c, \Delta E)$ varies with E_c only over a large energy scale. For systems similar to billiards, whose physical properties do not change much with energy, their physical properties do not vary significantly with E_c as long as it is not too close to the lowest quantum energy. For other systems with phase transition or other similar transition, the system does change significantly around the critical values. Consider water as an example. The physical property of water with E_c/k_B around the boiling temperature is very different from its property with E_c/k_B around the freezing temperature. However, for a quite large energy range between the freezing and boiling temperatures, water is just a normal liquid and its property does not change much. Therefore, the ratio $f(\wp, E_c, \Delta E)$ changes only when E_c is around these critical values. In Appendix E, the Aubry-André-Harper (AAH) model is used to illustrate this point. It is found that the ratio $f(\wp, E_c, \Delta E)$ changes significantly only when E_c is around the mobility edge.

For a quantum system with a well-defined classical counterpart, such self-similarity is rooted in the correspondence between the energy eigenstates and invariant distributions in classical phase space [28,41]. Without loss of generality, we choose $\wp = \hbar$ and focus on time-independent systems in the following discussion. By a well-defined classical counterpart, we mean that the quantum dynamics starting with a wave function that is well localized in phase space follows the classical trajectory in the semiclassical limit $\hbar \rightarrow 0$. In the Planck cell notation [38], such a correspondence can be written as

$$\lim_{\hbar \rightarrow 0} |\langle x' | \hat{U}(t) | x \rangle|^2 = \delta_{x', g_t x}, \quad (11)$$

in which $\hat{U}(t) = e^{-i\hat{H}t/\hbar}$ is the propagator of time evolution during t while g_t is the corresponding classical time evolution by canonical equations [42]. The basis $|x\rangle = |Q, P\rangle$ is the Planck cell basis at a discretized phase space [38]. As a result, for an energy eigenstate $|E\rangle$, we have

$$\lim_{\hbar \rightarrow 0} |\langle x | E \rangle|^2 = \lim_{\hbar \rightarrow 0} |\langle x | \hat{U}(t) | E \rangle|^2 = \lim_{\hbar \rightarrow 0} |\langle g_t^{-1} x | E \rangle|^2. \quad (12)$$

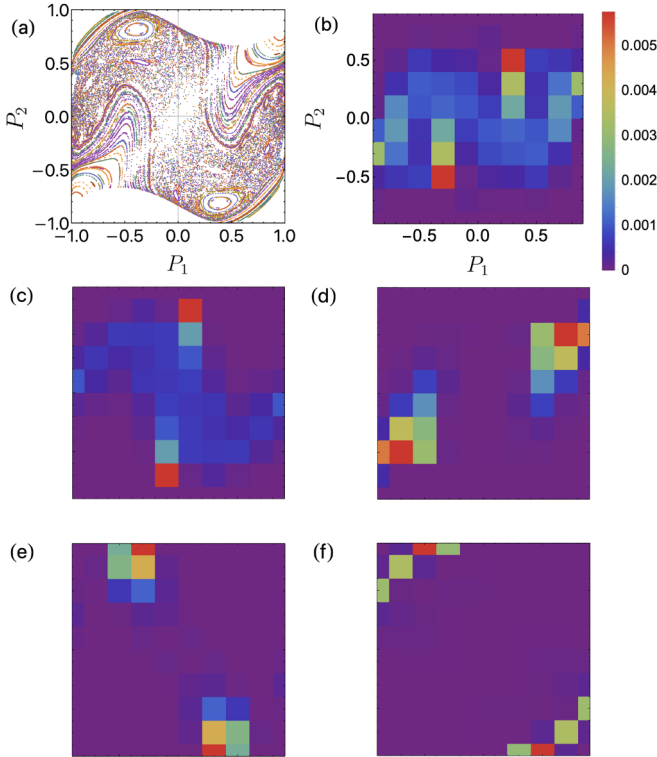


FIG. 7. (a) Poincaré sections for the classical coupled top model with energy $E_c = -0.9$. [(b)–(f)] are the 3194, 3196, 3198, 3202, and 3207th energy eigenstates (energy eigenvalues are -0.9018 , -0.9007 , -0.8998 , -0.8970 , -0.8939), respectively, in the quantum phase space. The parameters are $\mu = 0.5$ and $Q_1 = \pi$.

This shows that at the semiclassical limit, each energy eigenstate becomes a distribution in phase space which is invariant under classical dynamics [28,41].

For a classical system, its isoenergetic surface is usually filled with different invariant distributions, which do not overlap with each other [43]. The Poincaré sections in Figs. 7 and 9 offers some glimpses of such a structure: The invariant distributions represented by the chaotic seas do not overlap with the distributions represented by smooth lines in integral islands. Consider an energy shell \mathcal{S} with a very small width ΔE so that each isoenergetic surface within the shell is filled with similar nonoverlapping invariant distributions. In this way, with ΔE one can legitimately say that an invariant distribution occupies a volume in phase space. Due to the quantum-classical correspondence discussed above, these different invariant distributions are the limits of different energy eigenstates when \hbar goes to zero. As the energy is continuous in classical mechanics, the energy shell width ΔE can be arbitrary small. And for a given width ΔE , no matter how small it is, we can always choose a small -enough \hbar so that there are large number of eigenstates in the shell \mathcal{S} , in which the number of each type of eigenstates is proportional to the volume of the corresponding invariant distribution. This gives rise to the self-similarity that we have found in eigenstates.

Our above analysis has been done with quantum systems that have well-defined classical limits. However, such self-similarity appears very general and exists in all quantum

systems. This is indicated by our numerical computation in the next section, where a model of Heisenberg spin chain is studied. This system has no well-defined classical limit, and we still find self-similarity in its eigenstates. It is not clear why self-similarity exists in such quantum systems.

Before we present more examples, we use an analogy to summarize our finding. For a quantum system, if we regard each of its energy eigenstates as a small ball, then all the eigenstates lie on a one-dimensional line in the order of their corresponding eigenenergies. Such a line has at least one end, which is the ground state. Suppose that a fraction f of these balls are red, representing that the corresponding eigenstates have property A. We find that these red balls are thoroughly mixed with other balls. As a result, for any segment of line that contains large number of balls, the fraction of red balls on this segment is exactly f if we ignore the statistical fluctuations.

In quantum chaotic systems with no apparent symmetries, degeneracy rarely happens. People often refer to it as energy level repulsion. Our finding can also be regarded as a repulsion phenomenon: Energy eigenstates with similarity properties tend to “repel” each other and scatter rather evenly among other eigenstates. And this kind of repulsion exists for all quantum systems, not limited to chaotic systems.

III. EXAMPLES EXHIBITING SELF-SIMILARITY

Below are three examples. The first example, quantum coupled top, is a time-independent system; the second example, quantum kicked rotor, is a periodically driven system; the third example, a Heisenberg chain, is a quantum system that has no well-defined classical limit. Self-similarity in energy eigenstates is evident in all of them. The third examples suggests that the self-similarity exists also in quantum systems that have no well-defined classical limits.

A. Quantum coupled top

The quantum coupled top is a famous model that were used to study quantum chaos [44,45]. It describes the interaction between two identical angular momenta, \hat{L}_1 and \hat{L}_2 , which is governed by the following Hamiltonian [46,47]:

$$\hat{H} = \hat{L}_{1z} + \hat{L}_{2z} + \frac{\mu}{J} \hat{L}_{1x} \hat{L}_{2x}, \quad (13)$$

where J is the magnitude of the angular momentum and μ denotes the coupling constant.

This system has a well-defined classical counterpart, whose Hamiltonian is obtained by simply replacing the operators \hat{L}_1 and \hat{L}_2 with two variables of angular momentum, L_1 and L_2 . For the classical model, it is convenient to introduce a different set of canonical variables,

$$L_i = J(\sqrt{1 - P_i^2} \cos Q_i, \sqrt{1 - P_i^2} \sin Q_i, P_i), \quad (14)$$

where i is either 1 or 2. The classical Hamiltonian becomes

$$H = J(\sqrt{1 - P_1^2} \cos Q_1 + \sqrt{1 - P_2^2} \cos Q_2 + \mu P_1 P_2) \quad (15)$$

(rigorous derivation of quantum-classical correspondence is illustrated in Appendix B). The classical dynamics is

described by the following canonical equations:

$$\dot{P}_i = -\sqrt{1 - P_i^2} \sin Q_i, \quad \dot{Q}_i = \frac{P_i}{\sqrt{1 - P_i^2}} \cos Q_i + \mu P_j, \quad (16)$$

where $i, j \in \{1, 2\}$ and $i \neq j$. The classical dynamics is a mixture of regular and chaotic motions as indicated by the classical Poincaré section at $Q_1 = \pi$ with $\sin Q_2 > 0$ in Fig. 7(a). The parameters for the figure are $J = 2$, $\mu = 0.5$ and the energy $E_c = -0.9$.

To plot energy eigenstates in phase space, we first construct quantum phase space by dividing phase space into L^4 Plank cells, i.e., $Q_i = 0, \frac{2\pi}{L}, \dots, \frac{2\pi}{L}(L-1)$, and $P_i = \frac{-mL}{j}, \frac{-(m-1)L}{j}, \dots, \frac{mL}{j}$. Here $L = 2m + 1$ and $L^2 = 2j + 1$. Limited by computational resources, we take $L = 10$. For each Plank cell, we assign a localized quantum state [38,40,43]

$$|Q_1, P_1; Q_2, P_2\rangle = |Q_1, P_1\rangle \otimes |Q_2, P_2\rangle, \quad (17)$$

where $|Q, P\rangle$ is defined as [38]

$$|Q, P\rangle_j = \frac{1}{\sqrt{L}} \sum_{n=-m}^m e^{-iQ(n+Pj)} |n + Pj\rangle. \quad (18)$$

The subscript j means that Planck cells $|Q, P\rangle$ are dependent on angular momentum quantum number j . We will neglect j afterwards for simplicity. These quantum states not only form a complete basis for the system but also have excellent classical meaning: The average angular momentum of state $|Q, P\rangle$ is just the same as Eq. (14) and the uncertainties of J_x, J_y, J_z are all proportional to $\hbar\sqrt{j}$, which decreases as $1/\sqrt{\hbar}$ with decreasing \hbar and fixed J , see Appendix C.

As it is impossible to plot a complete energy eigenstate in the four-dimensional phase space, we plot a section, which we call quantum Poincaré section. In our calculation, for an energy eigenstate $|E\rangle$, we first set the section at $Q_1 = \pi$ and then compute the projection amplitude, $\rho_{Q,\text{sec}}(P_1, P_2; E) = |\langle \pi, P_1; Q_2, P_2 | E \rangle|^2$, where

$$Q_2 = \arccos \left[\frac{(H/J - \mu P_1 P_2 - \sqrt{1 - P_1^2} \cos Q_1)}{\sqrt{1 - P_2^2}} \right]. \quad (19)$$

The results $\rho_{Q,\text{sec}}$ for five different eigenstates are shown in Figs. 7(b)–7(f). The energy eigenvalues are chosen around $E = -0.9$, the energy for the classical Poincaré section in Fig. 7(a). It is clear that each quantum Poincaré section resembles a part of the classical Poincaré section. For example, Fig. 7(d) resembles integrable islands located at the upper right and lower left corners of Fig. 7(a), Fig. 7(c) corresponds to the whole chaotic sea in Fig. 7(a), and Fig. 7(e) resembles two integrable island located at the upper right and lower left corners of Fig. 7(a). The most interesting is that the five quantum Poincaré sections combined just fill up the classical Poincaré section. This feature is general in our numerical results: For any classical Poincaré section at a given energy E_c , we can always find energy eigenstates around E_c whose quantum Poincaré sections just fill up the classical Poincaré section. This feature is a signature of self-similarity in energy eigenstates.

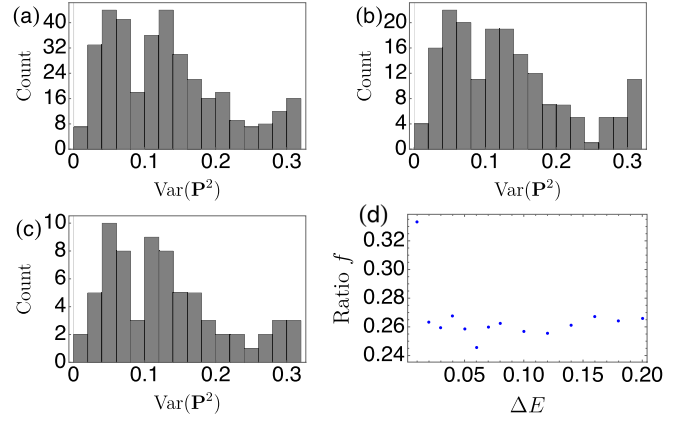


FIG. 8. Histograms the variance $\text{Var}(\mathbf{P}^2)$ at three different widths (a) $\Delta E = 0.2$, (b) $\Delta E = 0.1$, and (c) $\Delta E = 0.04$. (d) The ratio function $f(E_c, \Delta E)$ with the threshold $\delta = 0.16$. The energy shells are all centered at $E_c = -0.9$.

We next put the above observation on a quantitative ground by focusing on how wide the eigenstates spread in phase space. For an energy eigenstate $|E\rangle$ and its distribution $\rho_{Q,\text{sec}}$, we define the following variance:

$$\text{Var}(\mathbf{P}^2) \equiv \frac{\sum_{P_1} \sum_{P_2 \geq 0} \rho_{Q,\text{sec}}(\mathbf{P})(\mathbf{P} - \bar{\mathbf{P}})^2}{\sum_{P_1} \sum_{P_2 \geq 0} \rho_{Q,\text{sec}}(\mathbf{P})}, \quad (20)$$

where we abbreviate (P_1, P_2) as a vector \mathbf{P} and denote $\bar{\mathbf{P}}$ as the mean of \mathbf{P} for the left half of Poincaré section. If $|E\rangle$ is chaotic, then its $\text{Var}(\mathbf{P}^2)$ is large, while $\text{Var}(\mathbf{P}^2)$ will be small if it is regular. The classifier is defined as

$$C(\delta; |E\rangle) = \begin{cases} 0 & \text{if } 0 < \text{Var}(\mathbf{P}^2) < \delta \\ 1 & \text{if } \text{Var}(\mathbf{P}^2) \geq \delta \end{cases}, \quad (21)$$

where δ is a chosen threshold. For this classifier, the control parameter is ΔE , the width of the energy shell. Our numerical results are summarized in Fig. 8. The first three panels [Figs. 8(a)–8(c)] are the histograms of the variance for different widths ΔE . They are very similar to each other. In Fig. 8(d), the ratio function $f(E_c, \Delta E)$ in Eq. (10) is plotted, and it saturates quickly with ΔE . They all demonstrate the self-similarity in eigenstates.

For this model, the last numerical check is done by counting the numbers of integrable and chaotic eigenstates. We compute all the eigenstates in the energy shell $[-0.95, -0.85]$ and then examine each of them to see whether it is an integrable or chaotic eigenstate. We find that there are $N_I = 122$ integrable eigenstates and $N_C = 59$ chaotic ones. The volume of integrable islands and the total volume of the constant energy surface at $E_c = -0.9$ in classical phase space are evaluated numerically. Our result is $V_I/V = 0.60 \pm 0.02$, close to $N_I/(N_I + N_C) = 0.68$, confirming the self-similarity. For details, see Appendix D.

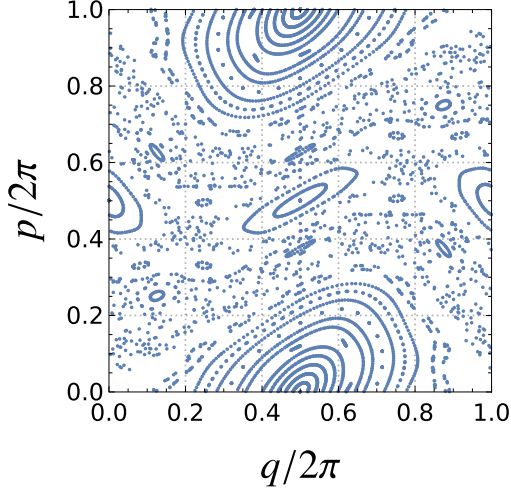


FIG. 9. The Poincaré section of the classical kicked rotor. The initial points are uniformly sampled along p axis with fixed q near π .

B. Quantum kicked rotor

The Hamiltonian of kicked rotor is [48]

$$H = \frac{p^2}{2} + K \cos q \sum_{n=-\infty}^{\infty} \delta(t - n), \quad (22)$$

where K is the kicking strength. Its classical dynamics can be reduced to the Chirikov map on the toric phase space $(q, p) \in [0, 2\pi]^{\otimes 2}$ by focusing the state before each kick, i.e., $(q_n, p_n) = (q, p)(t = n - 0)$. The dynamics reads [48]

$$\begin{cases} q_{n+1} = q_n + p_{n+1} & \text{mod } 2\pi, \\ p_{n+1} = p_n + K \sin q_n & \text{mod } 2\pi. \end{cases} \quad (23)$$

Parameter K controls the dynamics of kicked rotor. For $K \geq K_C \approx 0.972$ [48], the phase space is roughly separated into chaotic sea and integrable islands. See Fig. 9 for the case of $K = 1.1$.

As there is a periodic kicking, the quantum dynamics of the kicked rotor is given by the following unitary Floquet evolution:

$$\hat{U} = e^{-i\hat{p}^2/2\hbar} e^{-iK \cos \hat{q}/\hbar}. \quad (24)$$

The analogs to energy eigenstates and eigenvalues here are the eigenstates of \hat{U} (Floquet states) and their pseudoenergies [49–51]. For the continuity of notation, we still denote them as $|E\rangle$ and E , i.e., $\hat{U}|E\rangle = e^{-iE}|E\rangle$. We point out that there still holds the correspondence between Floquet states and the classical invariant distributions as we argued in Sec. II. This is illustrated in Fig. 10 with the same setup as in Refs. [38,40,52]. The phase space is discretized into $m \times m$ Planck cells and the effective Planck constant is $\hbar_{\text{eff}} = 2\pi \hbar/m^2$.

For this quantum kicked rotor, we discuss the self-similarity with two control parameters of \hbar_{eff} and the pseudoenergy shell width ΔE . The self-similarity with \hbar_{eff} is

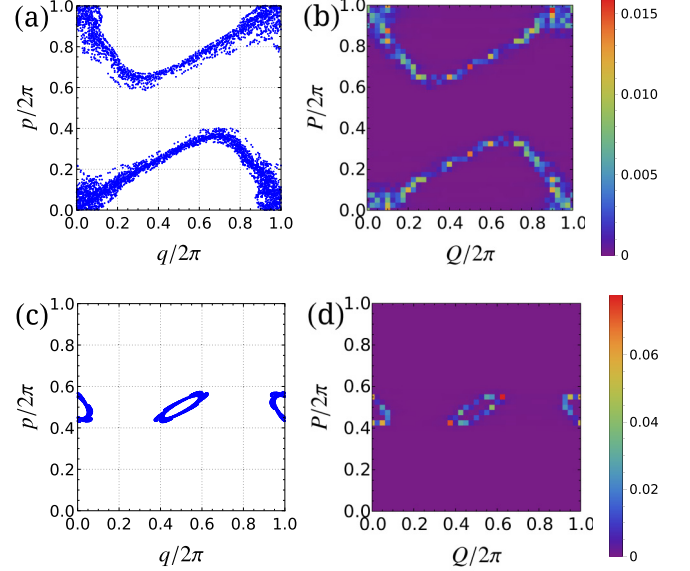


FIG. 10. The typical chaotic (a) and integrable (c) trajectories of classical kicked rotor and their corresponding quantum Floquet states [(b) and (d)]. The parameter $K = 1.1$ and the effective Planck constant is $\hbar_{\text{eff}} \approx 0.0039$, i.e., there are 40×40 Planck cells in total.

shown in Fig. 11(a) with the classifier

$$C_{\text{width}}(|E\rangle) = \begin{cases} 1 & W(|E\rangle) > 0.8\pi \\ 0 & \text{otherwise} \end{cases}. \quad (25)$$

Here $W(|E\rangle)$ is the width of Floquet state in phase space defined with Planck cell basis $|Q, P\rangle$ [38], i.e.,

$$W(|E\rangle)^2 = \sum_{Q,P} [(Q - \pi)^2 + (P - \pi)^2] |\langle Q, P | E \rangle|^2. \quad (26)$$

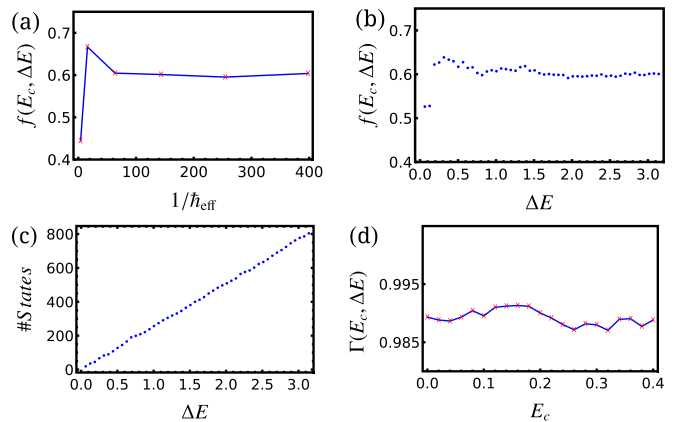


FIG. 11. The self-similarity with quantum kicked rotor. (a) The ratio $f(E_c, \Delta E)$ as a function of the inverse of the effective Planck constant with $\Delta E = 2$ and $E_c = 0$. (b) The ratio as the function of the width of energy shell ΔE with $\hbar_{\text{eff}} \approx 0.0039$ and $E_c = 0$. (c) The number of Floquet states as a function of the width of energy shell ΔE . (d) The dependence of the generalized Wigner–von Neumann entropy $\Gamma(E_c, \Delta E)$ on the center pseudoenergy E_c . The pseudoenergy shell width $\Delta E = 0.4$ here.

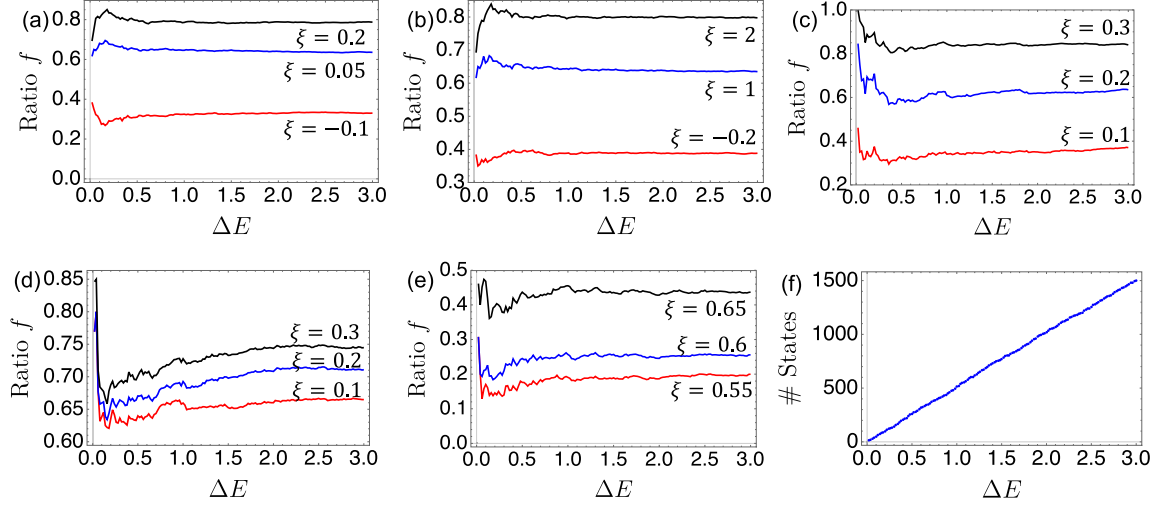


FIG. 12. The ratio f for various classifiers: (a) magnetization for a single spin (sixth spin), (b) total magnetization, (c) two-spin-correlation for third spin and fourth spin, (d) global-X-correlation, and (e) second Rényi entropy of first spin. (f) The total number of energy eigenstates in energy shell $[E_c - \Delta E/2, E_c + \Delta E/2]$. We take the length of spin chain to be $N = 12$, parameter $\rho = 0.4$ and central energy $E_c = 4$.

Geometrically, $W(|E\rangle)$ quantifies the “radius” of Floquet states to the center point $(q, p) = (\pi, \pi)$. With the same classifier, the self-similarity with pseudoenergy shell width ΔE as the control parameter is shown in Fig. 11(b), where the ratio $f(E_c, \Delta E)$ quickly saturates to a similar value as in Fig. 11(a). This demonstrates that decreasing \hbar_{eff} fixing ΔE is equivalent to increasing ΔE with fixed \hbar_{eff} as discussed in Appendix A.

Although the agreement between the two saturation values in Figs. 11(a) and 11(b) vindicates our argument in Appendix A, we note that our analysis in the Appendix only works at the vicinity of $\hbar \sim 0$ and for small ΔE , and the agreement at such large ΔE is still surprising. This is related to that the pseudoenergies are confined into $[0, 2\pi)$ due to the periodic kicking. This means that the different eigenenergies without kicking are folded into this finite interval. Thus the kicked rotor has the same dynamical feature at pseudoenergy shells centered at different pseudoenergies, similarly to the billiard systems where the dynamics is also not sensitive to the energy. This is supported by the results in Fig. 11(c), where the number of eigenstates in the energy shell grows linearly with the shell width. This can be further demonstrated by that the entropy of the renormalized distributions of Floquet states in given pseudoenergy shells is roughly independent of the center of the shell. Formally, we compute

$$p_{Q,P}(E_c, \Delta E) = \frac{\sum_{E' \in S(E_c, \Delta E)} |\langle Q, P|E'\rangle|^2}{|S(E_c, \Delta E)|}, \quad (27)$$

which is actually the probability distribution $p_{Q,P} = \text{Tr}[|Q, P\rangle\langle Q, P| \hat{\rho}(E_c, \Delta E)]$ of maximally mixed state in the energy shell $\hat{\rho}(E_c, \Delta E) \propto \sum_{E' \in S(E_c, \Delta E)} |E'\rangle\langle E'|$. We then compute its generalized Wigner–von Neumann entropy [53] on a Planck cell basis (with normalization),

$$\Gamma(E_c, \Delta E) = -\frac{1}{\log m^2} \sum_{Q,P} p_{Q,P}(E_c, \Delta E) \log p_{Q,P}(E_c, \Delta E). \quad (28)$$

The function \log is the natural logarithm. By normalization, we make sure $\Gamma \in [0, 1]$. In Fig. 11(d), that the entropy is almost constant as the center energy E_c changes demonstrates the independence of dynamics to E_c in the kicked rotor.

C. Heisenberg XXZ model

Though our explanation of self-similarity relies on the quantum-classical correspondence, we find that it exists for quantum systems that do not have well-defined classical limits. Here is an example, one-dimensional Heisenberg XXZ model [54], whose Hamiltonian with open boundary condition is

$$H = \sum_{i=1}^{N-1} (\sigma_i^x \sigma_{i+1}^x + \sigma_i^y \sigma_{i+1}^y + \rho \sigma_i^z \sigma_{i+1}^z), \quad (29)$$

where $\sigma_i^{x,y,z}$ are Pauli operators on the i th site. We use five different functions $F(|\psi_n\rangle)$ to characterize the energy eigenstates $|\psi_n\rangle$. The first four are expectations of different operators O , $F(O, |\psi_n\rangle) = \langle \psi_n | O | \psi_n \rangle$. These four different operators are as follows: (i) single spin, here we choose $\sigma_{[N/2]}^z$; (ii) total magnetization $M_z = \sum_{i=1}^N \sigma_i^z$; (iii) two-point correlation $C_{34} = \sigma_3^x \sigma_4^x$; and (iv) global-X-correlation product $N_x = \prod_{i=1}^N \sigma_i^x$. The fifth function the second-Rényi entropy [55] of the first spin, i.e.,

$$F(|\psi_n\rangle) = -\log [\text{Tr}(\rho_1^2)], \quad (30)$$

where $\rho_1 = \text{Tr}_{2,\dots,N} |\psi_n\rangle\langle \psi_n|$ is the reduced density matrix for the first spin. For each of these five different functions, the classifier is defined as

$$C(|\psi_n\rangle; \xi) = \begin{cases} 1 & F(|\psi_n\rangle) \geq \xi, \\ 0 & \text{otherwise,} \end{cases} \quad (31)$$

where ξ is a chosen threshold value.

All calculations are done by exact diagonalization and the results are shown in Fig. 12. For all the local operators [56],

the total magnetization, single spin and two-point-correlation operator, the ratio functions $f(\Delta E)$ quickly saturate as ΔE , indicating the self-similarity. The result for the the second-Rényi entropy is similar. However, for the global-X-correlation, the ratio does not saturate at a constant value even if there are hundreds of energy eigenstates in the energy shell. It seems that the self-similarity fails for nonlocal operators.

Our results can be interpreted in the context of observability of operators. When we observe a certain property of Heisenberg-XXZ spin chain in a macroscopic way, local properties, such as magnetization, correlation, or reduced density matrix for one spin, can be measured with macroscopic instruments. However, nonlocal operators such as global-X-correlation, do not have classical macroscopic, meaning and their properties cannot be measured with a classical instrument.

IV. CONCLUSION AND DISCUSSION

We have discovered self-similarity among energy eigenstates of a quantum system. If all the eigenstates are ordered according to their corresponding eigenvalues and are divided into different groups according to their properties or features, then the members of the same group tend to “repel” each other and scatter rather evenly among all the eigenstates. In other words, inside any energy shell $\mathcal{S}(E_c, \Delta E)$, the composition of eigenstates from different groups is very similar. Just like a shoreline, any piece looks similar to the other piece as long as the piece is not too short. We have offered an explanation why this self-similarity should exist in quantum systems that have well-defined classical limits. Our numerical results show that this self-similarity also exists in quantum systems that have no well-defined classical limits.

The three quantum systems that we studied in Sec. III have a common feature: Their Hilbert spaces have finite dimensions. When we enlarge their Hilbert spaces, for example, by increasing j (or N) or adding more spins, each of these quantum systems will have more eigenstates. The self-similarity suggests that despite that the Hilbert space is getting bigger, the composition of eigenstates will remain roughly the same. It is analog to shuffled cards: When you insert one deck of cards randomly into 100 decks of thoroughly shuffled cards, nothing changes significantly besides there are more cards. One may use this to define the classical limit of a quantum system, in particular, the quantum system that has no well-defined classical counterpart: When the composition of different types of eigenstates no longer changes with the dimension of the Hilbert space, the quantum system reaches its classical limit.

Modern statistical mechanics has a very basic hypothesis, the postulate of equal *a priori* probability [57]. It is regarded as a working hypothesis, that is, its justification comes not from that it is derived from the fundamental microscopic theory but from the fact that the conclusions derived from it agree with experiments [57]. The self-similarity among energy eigenstates offers a reasonable justification for this hypothesis from a microscopic perspective. According to this postulate, for a quantum system, the microcanonical ensemble average of any physical observable \hat{O}_{phy} should be

$\langle \hat{O}_{\text{phy}} \rangle_{\Delta E} = \text{Tr}[\hat{O}_{\text{phy}} \hat{\rho}_{\Delta E}]$ with

$$\hat{\rho}_{\Delta E} = \frac{1}{\Omega(E_c, \Delta E)} \left[\sum_{E \in \mathcal{S}} |E\rangle \langle E| \right], \quad (32)$$

where $\Omega(E_c, \Delta E)$ is the total number of energy eigenstates in the energy shell $\mathcal{S}(E_c, \Delta E)$. Let us project every eigenstate $|E\rangle$ into the phase space, then the probability of the system at the Planck cell $|Q, P\rangle$ is

$$\text{Prob}(Q, P) = \frac{1}{\Omega(E_c, \Delta E)} \left[\sum_{E \in \mathcal{S}} |\langle Q, P | E \rangle|^2 \right], \quad (33)$$

where Q and P are multidimensional variables. The self-similarity implies that this probability is zero outside of the shell $\mathcal{S}(E_c, \Delta E)$ and the same for every Planck cell in the shell. This holds for any quantum system, integrable or chaotic. For a fully chaotic system, every eigenstate $|E\rangle$ inside the shell looks about the same; consequently, the density matrix (32) is still valid even as the width ΔE is so small that there is only one eigenstate in the shell. This is just the well-known eigenstate thermalization hypothesis [58,59]. For systems that are not fully chaotic, the width ΔE has to be large enough so that different types of eigenstates are properly represented statistically. Overall, this explains why there is no need to consider the integrability of the system when the microcanonical density matrix (32) is used.

ACKNOWLEDGMENTS

This work is supported by the National Key R&D Program of China (Grant No. 2018YFA0305602), National Natural Science Foundation of China (Grant No. 11921005), and Shanghai Municipal Science and Technology Major Project (Grant No.2019SHZDZX01).

APPENDIX A: RELATION BETWEEN DECREASING PLANCK CONSTANT AND ENLARGING ENERGY WINDOW

When discussing the circular billiard, we have used the fact that the decreasing of \hbar is equivalent to simply increasing the shell width ΔE with fixed E_c . This is clearly right for the case of billiards; for a general case, it needs some more clarification.

Let us discuss the general case and the formal definition of the eigenstates in the energy shell here. Consider a general quantum system near the limit $\hbar \rightarrow 0$, the energy levels in the interval of $\mathcal{S}(E_c, \Delta E)$ could be expressed by a quantum number relative to E_c , i.e., by letting $E_c = E_{n_c}(\hbar)$, then $E_n(\hbar) = E_{n_c + (n - n_c)}(\hbar) \approx E_c + (n - n_c)^\beta \hbar^\alpha \equiv E_c + \hbar^\alpha G_{n - n_c}(E_c)$. Here $\alpha > 0$ and G_n is some function independent of \hbar . We note that the nearest energy spacing in a fixed energy shell $\mathcal{S}(E_c, \Delta E)$ should vanish as $\hbar \rightarrow 0$, and thus we always have the factor of \hbar^α . Here are two examples. For a one-dimensional billiard, we have $E_n \propto \hbar^2 n^2 \Rightarrow E_n \approx E_c + 2E_c \hbar^2 (n - n_c)$ with $\alpha = 2$. And for systems similar to hydrogen atoms, we have $E_n \propto 1/\hbar^2 n^2$ and thus $E_n \approx E_c - 2(n - n_c)\hbar/E_c^{3/2}$, which means $\alpha = 1$.

With the above consideration, the collection of eigenstates within a given energy shell can then be defined as

$$\begin{aligned} \Upsilon(E_c, \Delta E, \hbar) &= \{\psi_{n,\hbar} : E_n(\hbar) \in \mathcal{S}(E_c, \Delta E)\} \\ &= \{\psi_{n,\hbar} : \hbar^\alpha G_n \in \mathcal{S}(0, \Delta E)\}. \end{aligned} \quad (\text{A1})$$

With \hbar decreasing by a factor of $w > 1$, we have $\Upsilon(E_c, \Delta E, \hbar/w) = \{\psi_{n,\hbar/w}, \hbar^\alpha G_n/w^\alpha \in \mathcal{S}(0, \Delta E)\} = \{\psi_{n,\hbar/w}, \hbar^\alpha G_n \in \mathcal{S}(0, w^\alpha \Delta E)\}$. If the physics of eigenstates of fixed level is not sensitive to \hbar (this is true for quantum systems who have clear classical counterparts, since eigenstates become classical invariant distributions in phase space as $\hbar \rightarrow 0$), then we have the asymptotic behavior for the collection of eigenstates,

$$\Upsilon(E_c, \Delta E, \hbar/w) = \Upsilon(E_c, w^\alpha \Delta E, \hbar). \quad (\text{A2})$$

This means that changing \hbar and changing ΔE at the opposite directions are the same on the population of eigenstates, so does it on any statistical properties of eigenstates, e.g., the self-similarity.

This equivalence of increasing ΔE and decreasing \hbar relies on two assumptions. (1) The expansion of $E_{n_c+(n-n_c)} \approx E_c + \hbar^\alpha G_n$ near E_c has a high precision and (2) the eigenstates are not sensitive to \hbar . For billiards, both of these two assumptions are satisfied exactly. The energy levels has a natural cut-off at $\alpha = 2$ while the eigenfunction is actually the solution of $(\nabla^2 + k_{nm}^2)\psi_{nm} = 0$ which is independent of \hbar . For other systems discussed in the main text, these two assumptions are not exactly satisfied. For the double-top and kicked rotor, the equivalence still works well as their classical counterparts are well defined. For the XXZ model, we should expect that there is difference between enlarging ΔE and reducing \hbar .

We also note that the center of energy shell is the same on both sides of Eq. (A2). This holds when $E_c = E_{n_c}$ has a solution. In general, we can only choose n_c as the closest quantum energy level near E_c and this would make the right-hand side of Eq. (A2) has a different E_c . However, we expect when \hbar goes to zero, this shifting would vanish since the energy levels become sufficient dense and $E_c = E_{n_c}$ would has a solution of arbitrarily high precision.

APPENDIX B: CLASSICAL CORRESPONDENCE OF QUANTUM COUPLED TOP

We start with Hamiltonian (13) and use path integral method to rigorously derive the system's classical counterpart. We first review some basics of coherent states of spin J , which are defined as

$$|\mu\rangle = \frac{1}{(1+|\mu|^2)^J} \sum_{n=0}^{2J} \sqrt{\frac{(2J)!}{(2J-n)!n!}} \mu^n |L_z = J-n\rangle, \quad (\text{B1})$$

where $\mu = e^{i\phi} \tan(\theta/2)$. We have following properties for spin coherent states:

$$\langle \mu' | \mu \rangle = \frac{(1 + \mu'^* \mu)^{2J}}{(1 + |\mu'|^2)^J (1 + |\mu|^2)^J}, \quad (\text{B2})$$

$$\langle \mu' | \hat{L}_+ | \mu \rangle = \frac{2J\mu}{1 + \mu'^* \mu} \langle \mu' | \mu \rangle, \quad (\text{B3})$$

$$\langle \mu' | \hat{L}_z | \mu \rangle = J \frac{1 - \mu'^* \mu}{1 + \mu'^* \mu} \langle \mu' | \mu \rangle, \quad (\text{B4})$$

$$1 = \int \frac{2J+1}{4\pi} d\Omega |\mu\rangle \langle \mu|. \quad (\text{B5})$$

We want to evaluate the propagator $\langle \mu(t') | e^{-i\hat{H}T} | \mu(t) \rangle$ with $T = t' - t$. Here $\mu \equiv (\mu_1, \mu_2)$, $|\mu\rangle \equiv |\mu_1\rangle \otimes |\mu_2\rangle$, which corresponds a double-spin coherent state. We divide the time interval T into $N+1$ equal pieces of duration $\delta t = T/(N+1)$ and denote $\mu_i = \mu(t) + i\delta t$. After inserting N coherent-states' closure relations (B5), we get

$$\begin{aligned} &\langle \mu(t') | e^{-i\hat{H}T} | \mu(t) \rangle \\ &= \int \prod_{i=1}^N \left(\frac{2J+1}{4\pi} \right)^2 d\Omega_{1,i} d\Omega_{2,i} \langle \mu_{i+1} | e^{-i\hat{H}\delta t} | \mu_i \rangle \\ &= \int \mathcal{D}[\mu] \prod_{i=1}^N [\langle \mu_{i+1} | \mu_i \rangle - i \langle \mu_{i+1} | \hat{H} | \mu_i \rangle \delta t + \mathcal{O}(\delta t^2)] \\ &= \int \mathcal{D}[\mu] \prod_{i=1}^N \langle \mu_{i+1} | \mu_i \rangle \left\{ 1 - i\delta t \left[-\frac{2J \operatorname{Re} \mu_{1,i}}{1 + \mu_{1,i+1}^* \mu_{1,i}} \right. \right. \\ &\quad \left. \left. - (1 \leftrightarrow 2) - \mu J \frac{1 - \mu_{1,i+1}^* \mu_{1,i}}{1 + \mu_{1,i+1}^* \mu_{1,i}} \frac{1 - \mu_{2,i+1}^* \mu_{2,i}}{1 + \mu_{2,i+1}^* \mu_{2,i}} \right] \right\} \\ &= \int \mathcal{D}[\mu] \exp(iS[\mu(t), \mu(t')]). \end{aligned} \quad (\text{B6})$$

Here $\mathcal{D}[\mu] \equiv \prod_{i=1}^N \left(\frac{2J+1}{4\pi} \right)^2 d\Omega_{1,i} d\Omega_{2,i}$ is the functional integration measure, and $d\Omega_{1,i}$ ($d\Omega_{2,i}$) is the solid angle measure of the first (second) top at lattice μ_i . The discrete form of action immediately reads

$$\begin{aligned} \frac{S[\mu, \mu']}{2J} &= \sum_{i=1}^N -i \log \prod_{\alpha=1,2} \frac{1 + \mu_{\alpha,i+1}^* \mu_{\alpha,i}}{\sqrt{(1 + |\mu'_{\alpha}|^2)(1 + |\mu_{\alpha}|^2)}} \\ &\quad + \delta t \left(\frac{\operatorname{Re} \mu_{1,i}}{1 + \mu_{1,i+1}^* \mu_{1,i}} + \frac{\operatorname{Re} \mu_{2,i}}{1 + \mu_{2,i+1}^* \mu_{2,i}} \right. \\ &\quad \left. + \frac{\mu}{2} \frac{1 - \mu_{1,i+1}^* \mu_{1,i}}{1 + \mu_{1,i+1}^* \mu_{1,i}} \frac{1 - \mu_{2,i+1}^* \mu_{2,i}}{1 + \mu_{2,i+1}^* \mu_{2,i}} \right). \end{aligned} \quad (\text{B7})$$

In the continuous limit, substituting $\mu_{i+1} = \mu_i + d\mu$, we get

$$\frac{1 + \mu^* \mu}{\sqrt{(1 + |\mu'|^2)(1 + |\mu|^2)}} = 1 + \frac{1}{2} \frac{\mu d\mu^* - \mu^* d\mu}{1 + |\mu|^2}. \quad (\text{B8})$$

Then, the action can be written as the functional

$$\begin{aligned} \frac{S[\mu, \mu']}{J} &= \int dt \left[-i \frac{\mu_1 \dot{\mu}_1^* - \mu_1^* \dot{\mu}_1}{1 + |\mu_1|^2} - i \frac{\mu_2 \dot{\mu}_2^* - \mu_2^* \dot{\mu}_2}{1 + |\mu_2|^2} \right. \\ &\quad \left. + \cos \phi_1 \sin \theta_1 + \cos \phi_2 \sin \theta_2 + \mu \cos \theta_1 \cos \theta_2 \right]. \end{aligned} \quad (\text{B9})$$

The (normalized) Lagrangian reads

$$\begin{aligned} \mathcal{L} &= -(1 - \cos \theta_1) \dot{\phi}_1 - (1 - \cos \theta_2) \dot{\phi}_2 + \cos \phi_1 \sin \theta_1 \\ &\quad + \cos \phi_2 \sin \theta_2 + \mu \cos \theta_1 \cos \theta_2. \end{aligned} \quad (\text{B10})$$

In the classical limit, i.e., $J \rightarrow +\infty$ (or equivalently, $\hbar \rightarrow 0$), the propagator is permutation matrix with the jumping governed by the classical canonical equation of motion [Eq. (16)].

APPENDIX C: ANGULAR MOMENTUM PLANCK CELLS

In this Appendix, we give the proof of properties regarded to Planck cells [Eq. (18)]. Recall the definition of Planck cells [38]:

$$|Q, P\rangle = \frac{1}{\sqrt{\Delta_p}} \int_p^{P+\Delta_p} dp |p\rangle e^{-iQp/\hbar}, \quad (\text{C1})$$

where Δ_q and Δ_p are size of cells along q, p axis with $\Delta_q \Delta_p = 2\pi\hbar$. Express it in a discrete formalism, we obtain the Planck cells for a single angular momentum:

$$|Q, P\rangle = \frac{1}{\sqrt{L}} \sum_{n=-m+Pj}^{m+Pj} e^{-iQn} |L_z = n\rangle, \quad (\text{C2})$$

which is Eq. (18). It is unambiguous that the \hat{L}_z has mean value approximate to Pj while variation is in a same magnitude with m , i.e., proportional to $1/\sqrt{\hbar}$. In the classical limit, this form of Planck cell is equivalent to [38]

$$|Q, P\rangle^{(\text{position})} = \frac{1}{\sqrt{\Delta_q}} \int_Q^{Q+\Delta_q} dq |q\rangle e^{iPq/\hbar}, \quad (\text{C3})$$

which means the \hat{Q} also has mean value approximate to its classical correspondence with variation proportional to $1/\sqrt{\hbar}$. The above analysis can also be done by brute-force calculation using algebraic relations of quantum angular momentum.

APPENDIX D: COUPLED-TOP'S PHASE-SPACE VOLUME

Coupled-top's phase space is a four-dimensional manifold. Therefore the integrable islands and chaotic seas on a specific isoenergetic surface are three-dimensional hypersurface. However, only sections of isoenergetic surface are visible to us. In this part of Appendix, we show how to calculate the area of integrable islands and chaotic seas via plotting Poincaré sections (see Fig. 13). The overall integration measure for evaluating area of three-dimensional hypersurface Ω is

$$V(\Omega) = \int_0^{2\pi} dQ_1 A(\Omega; Q_1), \quad (\text{D1})$$

where

$$A(\Omega; Q_1) = \iint_{\mathbf{P} \in \Omega} dP_1 dP_2 C_1(E; Q_1, P_1, P_2) C_2(E; Q_1, P_1, P_2), \quad (\text{D2})$$

with two projection factors C_1 and C_2 defined as

$$C_1(E; Q_1, P_1, P_2) = \sqrt{1 + \left(\frac{\partial Q_2}{\partial P_1}\right)^2 + \left(\frac{\partial Q_2}{\partial P_2}\right)^2}, \quad (\text{D3})$$

$$C_2(E; Q_1, P_1, P_2) = \frac{1}{\sqrt{1 - \left(\frac{\partial H/\partial Q_1}{|VH|}\right)^2}}. \quad (\text{D4})$$

Here Q_2 is interpreted as a function of $(E; Q_1, P_1, P_2)$, see Eq. (19); and H is interpreted as a function of (Q_1, Q_2, P_1, P_2) with Q_2 evaluated via Eq. (19) after partial derivative. The three-dimensional area of region Ω can be approximated as a

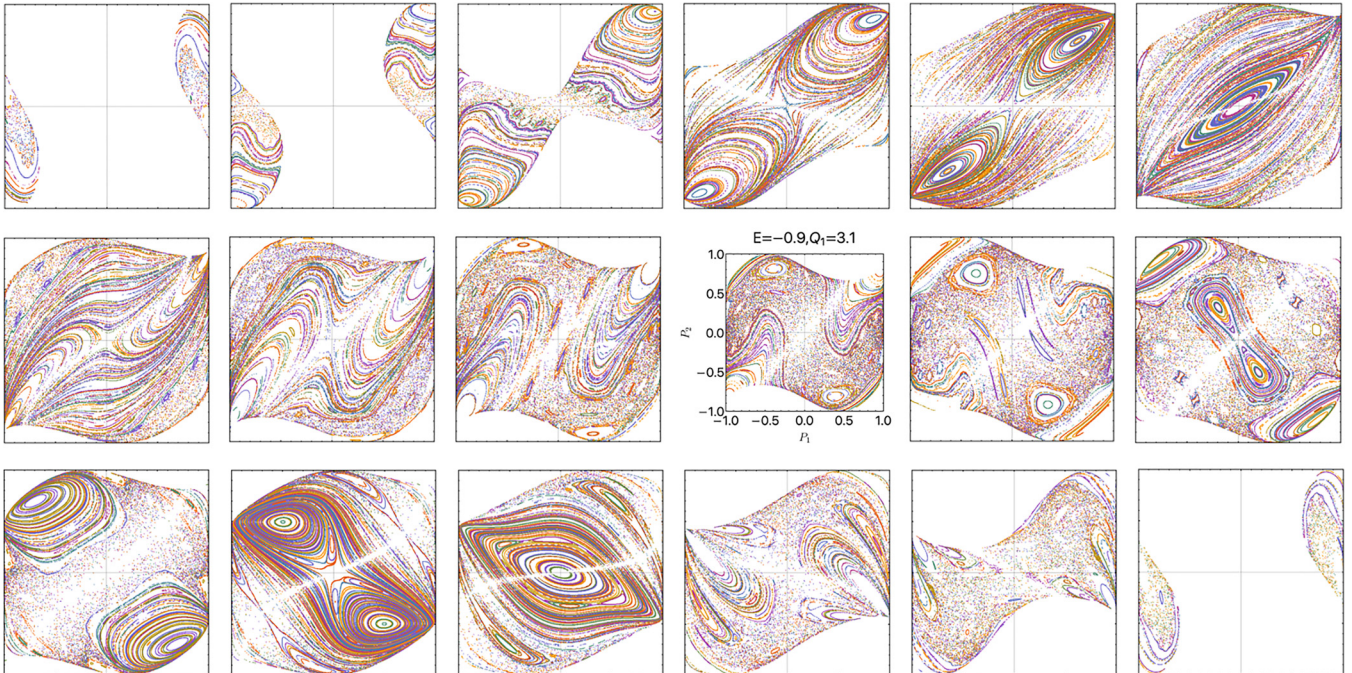


FIG. 13. The coupled-top's classical Poincaré sections of various Q_1 with $E = -0.9$ fixed. The partition we take is $\{0.1, 0.7, 1.0, 1.3, 1.6, 1.9, 2.2, 2.5, 2.8, 3.1, 3.4, 3.7, 4.0, 4.3, 4.6, 4.9, 5.2, 5.8\}$ (from left to right, up to down).

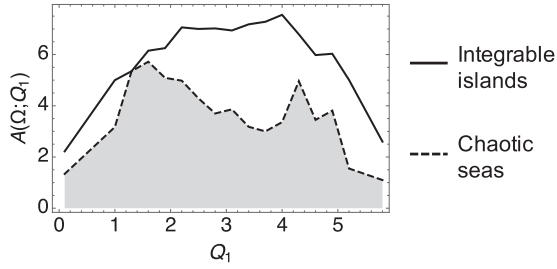


FIG. 14. Plot of integral $A(\Omega; Q_1)$. As for black line, Ω represents “total isoenergetic surface”; while for dashed line Ω denotes integrable islands.

summation

$$V(\Omega) \approx \sum_{i=1}^{N-1} \frac{A(\Omega, Q_{1,i}) + A(\Omega, Q_{1,i+1})}{2} \Delta Q_{1,i}, \quad (\text{D5})$$

where $\{Q_{1,1}, \dots, Q_{1,N}\}$ is a partition of $[0, 2\pi]$. The two-dimensional integral $A(\Omega; Q_1)$ is done in each Poincaré section numerically, and the results are plotted in Fig. 14.

APPENDIX E: ENERGY CENTER DEPENDENCE OF THE RATIO IN AAH MODEL

As discussed in Ref. [60], AAH model performs well mobility edge [60,61] as the parameters in model is properly chosen. Here we show the energy center, i.e., E_c dependence in such model. The numerical results are shown in Fig. 15.

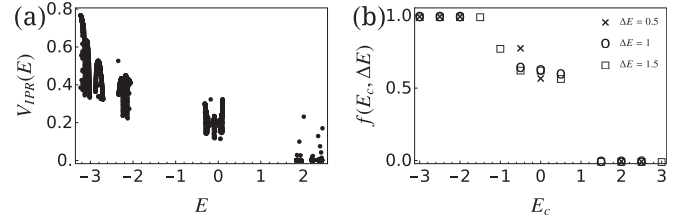


FIG. 15. The mobility edge and E_c dependence of ratio in AAH model. (a) The mobility edge indicated by inverse participation ratio of eigenstates at different energies. The parameters are $1/b = (\sqrt{5} - 1)/2$, $\alpha = 0.2$, $L = 3000$, and $\lambda = -1.1$. Theoretically the mobility edge is at $\mathcal{E} = 1$ as in Ref. [60]. (b) Different ratio $f(E_c, \Delta E)$ of E_c being above and below the mobility edge. Some points are missing for specific E_c and ΔE since there are gaps in this model.

The Hamiltonian of the model reads

$$\hat{H} = \sum_{n=1}^L |n\rangle\langle n+1| + \frac{\lambda \cos 2\pi nb}{1 - \alpha \cos 2\pi nb} |n\rangle\langle n| + \text{c.c.} \quad (\text{E1})$$

By letting $|L+1\rangle = |1\rangle$ we implement the periodic boundary condition. To quantitatively measure the locality of eigenstates and show the mobility edge, we use the inverse participation ratio (IPR) for each eigenstates as

$$V_{\text{IPR}}(|E\rangle) = \sum_{n=1}^L |\langle n|E\rangle|^4. \quad (\text{E2})$$

This quantity is also used in Ref. [60]. Note the eigenstates are normalized. The classifier is based on this function as

$$C(|E\rangle) = \begin{cases} 1 & V_{\text{IPR}}(|E\rangle) > 0.2 \\ 0 & \text{otherwise} \end{cases}. \quad (\text{E3})$$

- [1] H. Baltes, E. Hilf, and B. Institut, *Spectra of Finite Systems* (B.I.-Wissenschaftsverlag, Mannheim, 1976).
- [2] W. T. Lu, S. Sridhar, and M. Zworski, Fractal Weyl Laws for Chaotic Open Systems, *Phys. Rev. Lett.* **91**, 154101 (2003).
- [3] D. L. Shepelyansky, Fractal Weyl law for quantum fractal eigenstates, *Phys. Rev. E* **77**, 015202(R) (2008).
- [4] J. A. Ramilowski, S. D. Prado, F. Borondo, and D. Farrelly, Fractal Weyl law behavior in an open Hamiltonian system, *Phys. Rev. E* **80**, 055201(R) (2009).
- [5] J. M. Pedrosa, D. Wisniacki, G. G. Carlo, and M. Novaes, Short periodic orbit approach to resonances and the fractal Weyl law, *Phys. Rev. E* **85**, 036203 (2012).
- [6] M. Schönwetter and E. G. Altmann, Quantum signatures of classical multifractal measures, *Phys. Rev. E* **91**, 012919 (2015).
- [7] J. Wiersig and J. Main, Fractal Weyl law for chaotic microcavities: Fresnel’s laws imply multifractal scattering, *Phys. Rev. E* **77**, 036205 (2008).
- [8] M. Kopp and H. Schomerus, Fractal Weyl laws for quantum decay in dynamical systems with a mixed phase space, *Phys. Rev. E* **81**, 026208 (2010).
- [9] M. J. Körber, M. Michler, A. Bäcker, and R. Ketzmerick, Hierarchical Fractal Weyl Laws for Chaotic Resonance States in Open Mixed Systems, *Phys. Rev. Lett.* **111**, 114102 (2013).
- [10] A. Eberspächer, J. Main, and G. Wunner, Fractal Weyl law for three-dimensional chaotic hard-sphere scattering systems, *Phys. Rev. E* **82**, 046201 (2010).
- [11] T. A. Brody, J. Flores, J. B. French, P. A. Mello, A. Pandey, and S. S. M. Wong, Random-matrix physics: Spectrum and strength fluctuations, *Rev. Mod. Phys.* **53**, 385 (1981).
- [12] G. Montambaux, D. Poilblanc, J. Bellissard, and C. Sire, Quantum Chaos in Spin-Fermion Models, *Phys. Rev. Lett.* **70**, 497 (1993).
- [13] F. Haake, *Quantum Signatures of Chaos*, Springer Series in Synergetics (Springer, Berlin, 2013).
- [14] D. Szász-Schagrín, B. Pozsgay, and G. Takács, Weak integrability breaking and level spacing distribution, *SciPost Phys.* **11**, 037 (2021).
- [15] Y. Y. Atas, E. Bogomolny, O. Giraud, and G. Roux, Distribution of the Ratio of Consecutive Level Spacings in Random Matrix Ensembles, *Phys. Rev. Lett.* **110**, 084101 (2013).
- [16] C. Wang, P. Yan, and X. R. Wang, Non-Wigner-Dyson level statistics and fractal wave function of disordered Weyl semimetals, *Phys. Rev. B* **99**, 205140 (2019).
- [17] W.-J. Rao, Random matrix model for eigenvalue statistics in random spin systems, *Physica A* **590**, 126689 (2022).
- [18] J. v. Neumann, Beweis des ergodensatzes und desh-theorems in der neuen mechanik, *Z. Angew. Phys.* **57**, 30 (1929).

- [19] J. von Neumann, Proof of the ergodic theorem and the h-theorem in quantum mechanics, *Eur. Phys. J. H* **35**, 201 (2010).
- [20] D. Zhang, H. T. Quan, and B. Wu, Ergodicity and mixing in quantum dynamics, *Phys. Rev. E* **94**, 022150 (2016).
- [21] R. Aurich and F. Steiner, Statistical properties of highly excited quantum eigenstates of a strongly chaotic system, *Physica D* **64**, 185 (1993).
- [22] A. Bäcker, Random waves and more: Eigenfunctions in chaotic and mixed systems, *Eur. Phys. J.: Spec. Top.* **145**, 161 (2007).
- [23] H. Xiong and B. Wu, Universal behavior in quantum chaotic dynamics, *Laser Phys. Lett.* **8**, 398 (2011).
- [24] W. Beugeling, A. Bäcker, R. Moessner, and M. Haque, Statistical properties of eigenstate amplitudes in complex quantum systems, *Phys. Rev. E* **98**, 022204 (2018).
- [25] K. Clauß, F. Kunzmann, A. Bäcker, and R. Ketzmerick, Universal intensity statistics of multifractal resonance states, *Phys. Rev. E* **103**, 042204 (2021).
- [26] J. P. Keating and H. Ueberschär, Multifractal eigenfunctions for a singular quantum billiard, *Commun. Math. Phys.* **389**, 543 (2022).
- [27] S. W. McDonald and A. N. Kaufman, Wave chaos in the stadium: Statistical properties of short-wave solutions of the helmholtz equation, *Phys. Rev. A* **37**, 3067 (1988).
- [28] M. V. Berry, Regular and irregular semiclassical wavefunctions, *J. Phys. A: Math. Gen.* **10**, 2083 (1977).
- [29] C. M. Soukoulis and E. N. Economou, Fractal Character of Eigenstates in Disordered Systems, *Phys. Rev. Lett.* **52**, 565 (1984).
- [30] M. Sarkar, R. Ghosh, A. Sen, and K. Sengupta, Signatures of multifractality in a periodically driven interacting aubry-andré model, *Phys. Rev. B* **105**, 024301 (2022).
- [31] Y. Wang, C. Cheng, X.-J. Liu, and D. Yu, Many-Body Critical Phase: Extended and Nonthermal, *Phys. Rev. Lett.* **126**, 080602 (2021).
- [32] K. S. Tikhonov and A. D. Mirlin, Statistics of eigenstates near the localization transition on random regular graphs, *Phys. Rev. B* **99**, 024202 (2019).
- [33] L. F. Santos, F. Borgonovi, and F. M. Izrailev, Chaos and Statistical Relaxation in Quantum Systems of Interacting Particles, *Phys. Rev. Lett.* **108**, 094102 (2012).
- [34] M. Srdinšek, T. c. v. Prosen, and S. Sotiriadis, Signatures of Chaos in Nonintegrable Models of Quantum Field Theories, *Phys. Rev. Lett.* **126**, 121602 (2021).
- [35] A. Bäcker, M. Haque, and I. M. Khaymovich, Multifractal Dimensions for Random Matrices, Chaotic Quantum Maps, and Many-Body Systems, *Phys. Rev. E* **100**, 032117 (2019).
- [36] D. Babajanov, D. Matrasulov, Z. Sobirov, S. Avazbaev, and O. V. Karpova, Time-dependent quantum circular billiard, *Nanosyst.: Phys. Chem. Math.* **224** (2015).
- [37] A. Bäcker, R. Ketzmerick, S. Löck, M. Robnik, G. Vidmar, R. Höhmann, U. Kuhl, and H.-J. Stöckmann, Dynamical Tunneling in Mushroom Billiards, *Phys. Rev. Lett.* **100**, 174103 (2008).
- [38] Z. Wang, J. Feng, and B. Wu, Microscope for quantum dynamics with planck cell resolution, *Phys. Rev. Res.* **3**, 033239 (2021).
- [39] R. Pathria, *Statistical Mechanics*, International Series of Monographs in Natural Philosophy (Elsevier Science & Technology Books, Amsterdam, 1972).
- [40] C. Yin, Y. Chen, and B. Wu, Wannier basis method for the kolmogorov-arnold-moser effect in quantum mechanics, *Phys. Rev. E* **100**, 052206 (2019).
- [41] A. Knauf and Y. Sinai, *Classical Nonintegrability, Quantum Chaos*, Oberwolfach Seminars (Birkhäuser Basel, 2012).
- [42] K. Vogtmann, A. Weinstein, and V. Arnold, *Mathematical Methods of Classical Mechanics*, Graduate Texts in Mathematics (Springer, New York, 2010).
- [43] Z. Wang, Y. Wang, and B. Wu, Quantum chaos and physical distance between quantum states, *Phys. Rev. E* **103**, 042209 (2021).
- [44] M. Feingold and A. Peres, Regular and chaotic motion of coupled rotators, *Physica D* **9**, 433 (1983).
- [45] M. Feingold, N. Moiseyev, and A. Peres, Ergodicity and mixing in quantum theory. II, *Phys. Rev. A* **30**, 509 (1984).
- [46] D. Mondal, S. Sinha, and S. Sinha, Chaos and quantum scars in a coupled top model, *Phys. Rev. E* **102**, 020101(R) (2020).
- [47] D. Mondal, S. Sinha, and S. Sinha, Quantum transitions, ergodicity, and quantum scars in the coupled top model, *Phys. Rev. E* **105**, 014130 (2022).
- [48] B. Chirikov and D. Shepelyansky, Chirikov standard map, *Scholarpedia* **3**, 3550 (2008).
- [49] J. H. Shirley, Solution of the schrödinger equation with a hamiltonian periodic in time, *Phys. Rev.* **138**, B979 (1965).
- [50] H. Sambe, Steady states and quasienergies of a quantum-mechanical system in an oscillating field, *Phys. Rev. A* **7**, 2203 (1973).
- [51] J. M. Okuniewicz, Quasiperiodic pointwise solutions of the periodic, time dependent schrödinger equation, *J. Math. Phys.* **15**, 1587 (1974).
- [52] J. Jiang, Y. Chen, and B. Wu, Quantum ergodicity and mixing and their classical limits with quantum kicked rotor, [arXiv:1712.04533](https://arxiv.org/abs/1712.04533).
- [53] Z. Hu, Z. Wang, and B. Wu, Generalized Wigner–von Neumann entropy and its typicality, *Phys. Rev. E* **99**, 052117 (2019).
- [54] T. Schneider, E. Stoll, and U. Glaus, Excitation spectrum of planar spin-1/2 Heisenberg xxz chains, *Phys. Rev. B* **26**, 1321 (1982).
- [55] A. Rényi *et al.*, On measures of entropy and information, in *Proceedings of the Fourth Berkeley Symposium on Mathematical Statistics and Probability*, Contributions to the Theory of Statistics Vol. 1 (University of California Press, Berkeley, CA, 1961), pp. 547–561.
- [56] T. Albash and D. A. Lidar, Adiabatic quantum computation, *Rev. Mod. Phys.* **90**, 015002 (2018).
- [57] K. Huang, *Statistical Mechanics* (Wiley, New York, 1987).
- [58] L. D. Landau and E. Lifshitz, in *Statistical Physics*, 3rd ed., Part 1 (Butterworth-Heinemann, Oxford, 1980), p. 360.
- [59] M. Srednicki, Chaos and quantum thermalization, *Phys. Rev. E* **50**, 888 (1994).
- [60] S. Ganeshan, J. H. Pixley, and S. Das Sarma, Nearest Neighbor Tight Binding Models with an Exact Mobility Edge in One Dimension, *Phys. Rev. Lett.* **114**, 146601 (2015).
- [61] N. Mott, The mobility edge since 1967, *J. Phys. C* **20**, 3075 (1987).